Contrib Mineral Petrol (2013) 165:457–475
DOI 10.1007/s00410-012-0817-6

ORIGINAL PAPER

The control of cooling rate on titanomagnetite composition: implications for a geospeedometry model applicable to alkaline rocks from Mt. Etna volcano

Silvio Mollo · Keith Putirka · Gianluca Iezzi · Piergiorgio Scarlato

Received: 19 March 2012 / Accepted: 21 September 2012 / Published online: 6 October 2012

Abstract In this study, we have investigated the control of cooling rate on the composition of titanomagnetite formed from a trachybasaltic melt. Results show that disequilibrium growth conditions exert a primary control on the abundance, texture, and composition of the crystals. As the degree of cooling is increased, titanomagnetites show immature textures and are progressively enriched in Al + Mg and depleted in Ti. Thus, early-formed titanomagnetite nuclei do not re-equilibrate with the melt over faster cooling rates; instead, their compositions are far from equilibrium. On the basis of the different intra-crystal redistribution rates for Ti, Al, and Mg, we have calibrated a geospeedometer that represents the first quantitative description of the effect of cooling rate on titanomagnetite composition. This model was tested using the compositions of titanomagnetites in lava and dike samples from Mt. Etna volcano whose crystallization conditions resemble those of our experiments. Cooling rates calculated for lava samples are comparable with those measured in several volcanic complexes. At Mt. Etna, compositional variations of titanomagnetite grains from the innermost to the outermost part of a dike testify to progressively higher degrees of cooling, in agreement with numerical simulations of thermal gradients in and around magmatic intrusions.

Keywords Titanomagnetite · Cooling rate · Geospeedometry model · Mt. Etna

Communicated by T. L. Grove.

Electronic supplementary material The online version of this article (doi:10.1007/s00410-012-0817-6) contains supplementary material, which is available to authorized users.

S. Mollo (✉) · P. Scarlato
Istituto Nazionale di Geofisica e Vulcanologia,
Via di Vigna Murata 605, 00143 Rome, Italy
e-mail: mollo@ingv.it

K. Putirka
Department of Earth and Environmental Sciences,
California State University, Fresno, 2576 E. San Ramon Avenue,
MS/ST25, Fresno, CA 93740-8039, USA

G. Iezzi
Dipartimento DIGAT, Università G. d'Annunzio,
Via Dei Vestini 30, 66013 Chieti, Italy

Introduction

Titanomagnetite is a common accessory mineral in many igneous rocks (Toplis and Carroll 1995; Jang et al. 2001; Freda et al. 2008). At temperatures above 600 °C, titanomagnetite exhibits a complete solid solution of two end-members, that is, magnetite (Mt; Fe_3O_4) and ulvöspinel (Usp; Fe_2TiO_4). This solid solution is described as $Fe_{3-x}Ti_xO_4$, where $0 < x < 1$ is the proportion of Usp formed by the replacement of two Fe^{3+} cations by Fe^{2+} and Ti^{4+} (Putnis 1992; Bosi et al. 2009; Pearce et al. 2010 and references therein).

The amount of Usp plays a major role in controlling rock magnetism and the paleomagnetic properties of the Earth's crust (O'Reilly 1984; Banerjee 1991; Pick and Tauxe 1994; Zhou et al. 2000; Bowles et al. 2011). At room temperature, pure Mt is ferromagnetic, whereas pure Usp is paramagnetic. As a result, higher contents of Usp component in titanomagnetite cause lower magnetic susceptibilities, lower saturation magnetization, and lower spontaneous magnetization and Curie temperatures of the hosting rocks (Lattard et al. 2006; Chadima et al. 2009). For this reason, the knowledge and quantification of factors

controlling the amount of Usp are of fundamental importance for paleomagnetic studies (e.g. Zhou et al. 2000).

A wealth of experimental investigators have documented that the chemistry of titanomagnetite changes in response to variations in melt composition, temperature, and oxygen fugacity (Spencer and Lindsley 1981; Juster et al. 1989; Ghiorso and Sack 1991; Scaillet and Evans 1999; Toplis and Carroll 1995; Thy et al. 2006). However, there is now recognition that igneous crystals may grow rapidly during cooling and, in the process, may deviate from equilibrium (Hammer 2008 and references therein). Accordingly, studies dealing with pillows of mid-ocean ridge basalts (MORBs), lava flows, and dikes have demonstrated, by means of chemical and magnetic measurements, that the Usp content in titanomagnetite is significantly dependent on the kinetic conditions of the system (e.g. Smith and Prévot 1977; Zhou et al. 2000; Kissel et al. 2010; Mollo et al. 2011a, 2012a). Large and euhedral Ti-rich titanomagnetites are found in the innermost and less efficiently cooled parts of pillows, dikes, and lava flows, whereas tiny and dendritic Ti-poor crystals are observed near the outermost and rapidly cooled portions. These observations have also been recently corroborated by kinetically controlled experiments on Fe-rich basaltic (Hammer 2006) and andesitic (Iezzi et al. 2011) melts.

However, although several studies have experimentally quantified the effect of cooling rate on the composition of some important silicate phases, such as, clinopyroxene and plagioclase (Muncill and Lasaga 1987; Lofgren et al. 2006; Hammer 2008; Iezzi et al. 2008, Mollo et al. 2010a, 2011b, 2012b), there has been no investigation focused on the compositional variation of titanomagnetite.

In order to remedy this paucity of information, we present new data on the variation of Ti and other minor components, such as, Al and Mg, in titanomagnetite as a function of cooling rate. Titanomagnetite crystals were grown from a trachybasaltic melt commonly characterizing the magmatic activity of Mt. Etna volcano (Italy). The experiments were conducted at 0.1 and 500 MPa to reproduce both sub-aerial and sub-volcanic magma emplacement conditions. Indeed, eruptive activity at Mt. Etna typically occurs through (1) summit lava flow emissions fed by the central conduit and (2) lateral events triggered by deep tectonic fracturing that allows dike-like intrusions to propagate from ≥11-km depth up to the surface (Corsaro et al. 2009). This means that magma does not only cool at sub-aerial conditions, but it also solidifies at depth originating as a complex system of dike intrusions (Mollo et al. 2011a, c). Three different experimental sets were performed over the buffering conditions of NNO + 1.5: (1) cooling rate experiments of 0.5, 2.1, 3, 9.4, and 15 °C/min from 1,250 down to 1,000 °C, (2) quenching temperature experiments of 1,025, 1,050, 1,075, 1,090, and 1,100 °C at the fixed cooling rate of 0.5 °C/min, and (3) isothermal temperature experiments of 1,000, 1,025, 1,050, 1,075, 1,090, and 1,100 °C. The compositional variations measured for titanomagnetites allowed us to calibrate a geospeedometer based on the kinetically controlled cation redistributions in the crystals. This model was tested on natural alkaline samples from lava flows and dikes outcropping at Mt. Etna volcano. Results show cooling rates that are in good agreement with those determined by means of different geospeedometers and thermal models.

Starting material, experiments, and analyses

All experiments and analyses were carried out at the HP-HT Laboratory of Experimental Volcanology and Geophysics of the Istituto Nazionale di Geofisica e Vulcanologia in Roma (Italy). The chemistry of the synthetic starting material used for the experiments corresponds to a basaltic lava erupted in 2001 from Mt. Etna volcano. This starting material was synthesized by mixing oxide and carbonate powders in a ball mill. The resulting mixture was melted twice, to ensure the homogeneity of the glass using a Pt-crucible loaded in 1-atm furnace at 1,600 °C for 3 h. The glass was analyzed by X-ray powder diffraction and scanning electron microscopy, and no crystalline phases were detected (see also Del Gaudio et al. 2010 for further details). Twenty microprobe analyses of this glass yielded an average composition (in wt%) of SiO_2 = 47.61 (±0.35), TiO_2 = 1.65 (±0.4), Al_2O_3 = 16.76 (±0.21), FeO = 10.58 (±0.12), MnO = 0.17 (±0.02), MgO = 6.51 (±0.12), CaO = 11.13 (±0.14), Na_2O = 3.31 (±0.07), K_2O = 1.82 (±0.04), and P_2O_5 = 0.46 (±0.04).

High-pressure experiments were performed at 500 MPa in a piston cylinder apparatus. Fe-presaturated Pt-capsules loaded with the starting powder were positioned into a 19.1-mm NaCl–crushable alumina–pyrophyllite–Pyrex assembly which produces a fO_2 during the experiments of NNO + 1.5 (see also Freda et al. 2008; Mollo et al. 2010b).

Atmospheric pressure experiments were performed in a vertical tube gas-mixing furnace. Fe-presaturated Pt-capsules loaded with the starting powder were suspended within the furnace where a flux of CO/CO_2 gas mixture imposed a buffering condition of NNO + 1.5. Oxygen fugacity was monitored and maintained constant over the experimental temperatures by means of an yttria-doped-zirconia solid electrolyte oxygen sensor ($SIRO_2$, Ceramic Oxide Fabricators, Ltd., Australia) and two digital thermal mass flow meters controlled via software. Following Tormey et al. (1987), the experiments were performed under a partial pressure of sodium (in the form of Na_2SiO_3) in the

furnace atmosphere to minimize the sodium loss in the melt.

Our experiments at both 500 and 0.1 MPa can be divided into three sets (Table 1). Experimental Set 1 was designed to quantify the systematic changes in titanomagnetite composition due to cooling rate; the samples were cooled using five rates of 15, 9.4, 3, 2.1, and 0.5 °C/min from 1,250 down to 1,000 °C. As determined by Del Gaudio et al. (2010), 1,250 °C is a superliquidus temperature and is 39 °C higher than the liquidus temperature (1,211 °C) of the trachybasalt. Experimental Set 2 was performed to track the role of crystallization path on the titanomagnetite crystal chemistry; the samples were cooled at the fixed cooling rate of 0.5 °C/min using five different quenching temperatures of 1,025, 1,050, 1,075, 1,090, and 1,100 °C. For both Experimental Set 1 and 2, the superliquidus temperature of 1,250 °C was achieved starting from room temperature with a ramp of 100 °C/min which was then maintained for 30 min. According to nucleation theory, nucleation energy barriers scale with melt structure that, in turn, changes as a function of the thermal pretreatment of the starting material (Hammer 2008). As both the experimental duration and the superliquidus temperature are increased, the melt is progressively depolymerized, decreasing the quantity of large clusters that can become nuclei (Hammer 2008). Our study uses the assumption that, at magma chamber conditions and over the time scale of magmatic processes, the melt is in equilibrium with coexisting titanomagnetite crystals (i.e. the melt structure is fully relaxed). Therefore, compositional variations of titanomagnetites are mainly driven by dynamic crystallization conditions during magma emplacement. In this view, we need apply pre-heating conditions (i.e. 1,250 °C and 30 min) such that within our experiments, temperatures were sufficient for the destruction of pre-existing melt structures. To test this, we have performed two additional experiments at atmospheric pressure. Experiments were cooled from 1,400 °C down to 1,000 °C using a rate of 15 and 0.5 °C/min (Table 1). The superliquidus temperature was achieved (and then maintained for 180 min) starting from room temperature with a ramp of 100 °C/min. It is worth stressing that Tsuchiyama (1983) have demonstrated that both the heating duration of 180 min and temperature of 1,400 °C are higher than those required to achieve equilibrium in primitive silicate melts. Furthermore, Kirkpatrick et al. (1979) and Muncill and Lasaga (1987) have pointed out that when equilibrium is attained, no differences are observed in results from crystal-growth experiments with crystalline starting materials or reheated quenched glasses. By comparing run products obtained using thermal pre-treatments of 1,250 °C (30 min) and 1,400 °C (180 min), we did not observed significant variations, for example, no delay of crystal nucleation and no change in phase assemblage and phase proportion (Table 1). Consequently, crystalline precursors (e.g. embryonic clusters that can become nuclei) did not survive to thermal pre-treatments. We can conclude that, at 1,250 °C, the relaxation time to reach equilibrium would be much higher than the 30 min used for the trachybasaltic melt, in agreement with the general observation that relaxation kinetics of the melt are extremely rapid in time (i.e. from milli- to micro-seconds) at superliquidus temperatures (Richet 2002; Webb 2005; Dingwell 2006). Experimental Set 3 was carried out in order to asses the compositions of titanomagnetites under equilibrium conditions; six samples were heated from room temperature up to 1,000, 1,025, 1,050, 1,075, 1,090, and 1,100 °C, holding the final temperature constant for 42 h. To test the achievement of equilibrium, two reversal experiments were also performed at atmospheric pressure (Table 1). The sample was heated from room temperature up to 1,250 °C, which was maintained for 30 min. The superliquidus temperature was decreased using a rate of 15 °C/min to the target temperature (i.e. 1,000 and 1,100 °C) which was then held constant for 42 h.

Chemical analyses were conducted with a JEOL-JXA8200 EDS-WDS combined electron microprobe equipped with five wavelength-dispersive spectrometers, using a 15 kV accelerating voltage and 10 nA beam current. Crystals were analyzed with a beam size of 2 μm and a counting time of 20 and 10 s on peaks and background, respectively. The following standards have been adopted for the various chemical elements: jadeite (Si and Na), corundum (Al), forsterite (Mg), andradite (Fe), rutile (Ti), orthoclase (K), barite (Ba), apatite (P), and spessartine (Mn). Sodium and potassium were analyzed first to reduce possible volatilization effects. Precision was better than 5 % for all cations. Images were obtained with a JEOL FE-SEM 6500F equipped with an energy dispersion microanalysis system.

Results

Run products obtained at 500 and 0.1 MPa show comparable phase assemblages and textural features (Table 1 and Fig. 1). Plagioclase, clinopyroxene, and titanomagnetite occur in all charges with an almost constant ratio of 1.5:1:0.2. The melt is present in each run product and its abundance increases with increasing temperature and cooling rate.

In detail, as the cooling rate is increased from 0.5 to 15 °C/min, the amount of crystals in run products decreases from 81 to 14 vol.%; in addition, as the quenching and isothermal temperatures are increased from 1,000 to

Table 1 Run conditions and phases occurring in experimental products

Run#	Cooling rate (°C/min)	Initial temperature (°C)	Final temperature (°C)	fO_2 (buffer)	Pressure (MPa)	Phases(vol. %)
Variable cooling rate						
EB1D	0.5	1,250	1,000	NNO + 1.5	500	cpx(31) + plg(46) + timt(3) + gl(19)
EB8A	2.1	1,250	1,000	NNO + 1.5	500	cpx(29) + plg(44) + timt(3) + gl(24)
EB1E	3.0	1,250	1,000	NNO + 1.5	500	cpx(25) + plg(26) + timt(3) + gl(46)
EB7B	9.4	1,250	1,000	NNO + 1.5	500	cpx(13) + plg(19) + timt(2) + gl(66)
EB1F	15	1,250	1,000	NNO + 1.5	500	cpx(12) + plg(8) + timt(1) + gl(79)
EB1VF	0.5	1,250	1,000	NNO + 1.5	0.1	cpx(27) + plg(40) + timt(4) + gl(29)
EB2VF	2.1	1,250	1,000	NNO + 1.5	0.1	cpx(24) + plg(38) + timt(4) + gl(34)
EB3VF	3.0	1,250	1,000	NNO + 1.5	0.1	cpx(11) + plg(20) + timt(3) + gl(66)
EB4VF	9.4	1,250	1,000	NNO + 1.5	0.1	cpx(10) + plg(21) + timt(2) + gl(67)
EB5VF	15	1,250	1,000	NNO + 1.5	0.1	cpx(5) + plg(7) + timt(2) + gl(86)
EB18VF	0.5	1,400	1,000	NNO + 1.5	0.1	cpx(25) + plg(41) + timt(4) + gl(30)
EB19VF	15	1,400	1,000	NNO + 1.5	0.1	cpx(6) + plg(9) + timt(2) + gl(83)
Variable quenching temperature						
EB1D	0.5	1,250	1,000	NNO + 1.5	500	cpx(31) + plg(46) + timt(3) + gl(19)
EB12A	0.5	1,250	1,025	NNO + 1.5	500	cpx(14) + plg(25) + timt(1) + gl(60)
EB13A	0.5	1,250	1,050	NNO + 1.5	500	cpx(14) + plg(15) + timt(1) + gl(69)
EB14A	0.5	1,250	1,075	NNO + 1.5	500	cpx(7) + plg(11) + timt(2) + gl(80)
EB10A	0.5	1,250	1,090	NNO + 1.5	500	cpx(4) + plg(4) + timt(1) + gl(91)
EB11B	0.5	1,250	1,100	NNO + 1.5	500	cpx(7) + plg(5) + timt(1) + gl(87)
EB6VF	0.5	1,250	1,000	NNO + 1.5	0.1	cpx(27) + plg(40) + timt(4) + gl(29)
EB7VF	0.5	1,250	1,025	NNO + 1.5	0.1	cpx(10) + plg(20) + timt(2) + gl(68)
EB8VF	0.5	1,250	1,050	NNO + 1.5	0.1	cpx(10) + plg(12) + timt(2) + gl(76)
EB9VF	0.5	1,250	1,075	NNO + 1.5	0.1	cpx(5) + plg(11) + timt(2) + gl(82)
EB10VF	0.5	1,250	1,090	NNO + 1.5	0.1	cpx(4) + plg(7) + timt(2) + gl(87)
EB11VF	0.5	1,250	1,100	NNO + 1.5	0.1	cpx(4) + plg(7) + timt(2) + gl(87)
Variable isothermal temperature						
EB9A	–	1,000	1,000	NNO + 1.5	500	cpx(33) + plg(47) + timt(4) + gl(17)
EB17A	–	1,025	1,025	NNO + 1.5	500	cpx(19) + plg(29) + timt(3) + gl(50)
EB18A	–	1,050	1,050	NNO + 1.5	500	cpx(17) + plg(20) + timt(3) + gl(61)
EB19A	–	1,075	1,075	NNO + 1.5	500	cpx(10) + plg(16) + timt(3) + gl(72)
EB20A	–	1,090	1,090	NNO + 1.5	500	cpx(9) + plg(11) + timt(2) + gl(78)
EB21A	–	1,100	1,100	NNO + 1.5	500	cpx(8) + plg(10) + timt(2) + gl(80)
EB12VF	–	1,000	1,000	NNO + 1.5	0.1	cpx(27) + plg(41) + timt(3) + gl(29)
EB12VF-R	–	1,000	1,000	NNO + 1.5	0.1	cpx(26) + plg(39) + timt(4) + gl(31)
EB13VF	–	1,025	1,025	NNO + 1.5	0.1	cpx(16) + plg(25) + timt(3) + gl(56)
EB14VF	–	1,050	1,050	NNO + 1.5	0.1	cpx(9) + plg(14) + timt(2) + gl(75)
EB15VF	–	1,075	1,075	NNO + 1.5	0.1	cpx(7) + plg(12) + timt(2) + gl(80)
EB16VF	–	1,090	1,090	NNO + 1.5	0.1	cpx(5) + plg(10) + timt(2) + gl(83)
EB17VF	–	1,100	1,100	NNO + 1.5	0.1	cpx(5) + plg(9) + timt(2) + gl(84)
EB17VF-R	–	1,100	1,100	NNO + 1.5	0.1	cpx(6) + plg(10) + timt(1) + gl(83)

1,100 °C, the crystal content progressively decreases from 83 to 16 vol.% and from 81 to 13 vol.%, respectively (Table 1). In the following, we focus on the effect of cooling rate on the textural and compositional variations of titanomagnetite crystals; the morphological and chemical features of clinopyroxene and plagioclase have been extensively discussed in Del Gaudio et al. (2010) and Mollo et al. (2010a, b).

Titanomagnetite texture

Irrespective of temperature and pressure conditions, cooling rate exerts the primary control on the morphology of titanomagnetite crystals (Fig. 1). In general, experiments cooled more rapidly than 2.1 °C/min contain tiny crystals that form texturally immature dendrites with side branches growing from the major dendrite arms (Fig. 1a, b, c), whereas, at lower cooling rates, cruciform anhedral crystals are progressively replaced by sub-euhedral titanomagnetites (Fig. 1d, e, f).

This textural maturation also includes the following: (1) at 15 °C/min, crystals have swallowtail (or dendritic) shapes with a limited number of developed planar faces (Fig. 1a), (2) at 9, 3, and 2.1 °C/min, titanomagnetites show swallowtail and hopper (or skeletal) shapes with a significant number of well developed faceted edges (Fig. 1b, c, d), and (3) at 0.5 °C/min and at the isothermal temperature of 1,000 °C, titanomagnetites are characterized by nearly well-formed planar rims with a few to no hopper inclusions, that is, a quasi-mature texture (Fig. 1e, f).

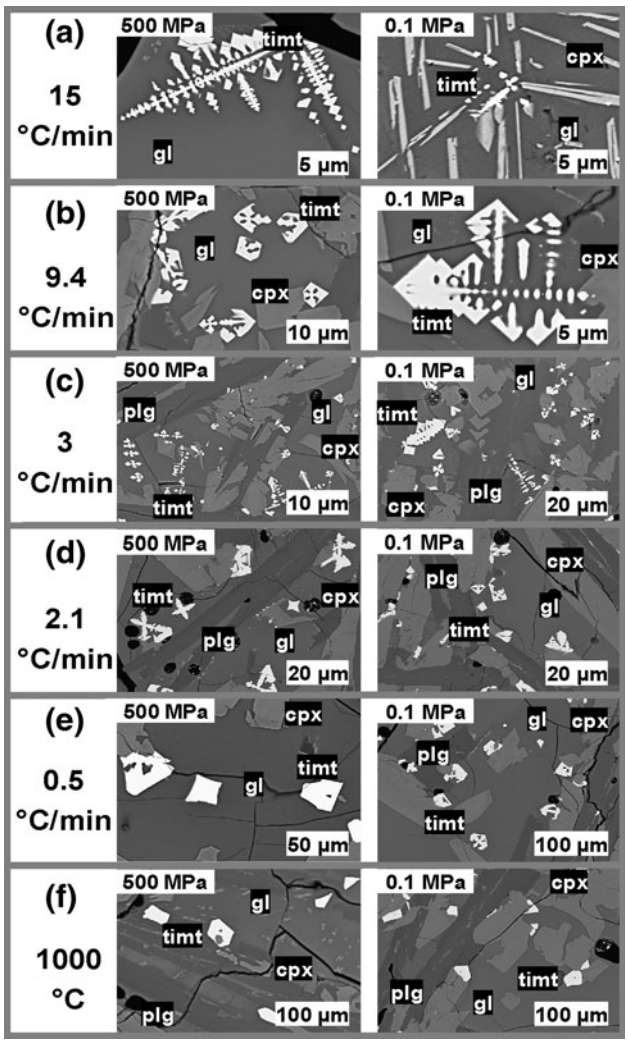

Fig. 1 Textural features of titanomagnetites formed at 500 and 0.1 MPa from run products cooled from 1,250 to 1,000 °C at 15 (**a**), 9.4 (**b**), 3 (**c**), 2.1 (**d**), 0.5 (**e**) °C/min and from run products kept at the isothermal temperature of 1,000 °C (f). *Plg* plagioclase, *Cpx* clinopyroxene, *Timt* titanomagnetite, *Gl* glass

Titanomagnetite composition

In Table 2, the average titanomagnetite composition is reported for each experimental run (see also Table 1S available as supplementary material). The crystal chemical formulas are recalculated following Stormer (1983): (1) we calculated the molar proportions of all cations in the analyses; (2) the cations were normalized to a formula unit of 3 sites; (3) we calculated the sum of the cationic charges per formula unit and subtracted 8; (4) the charge deficiency was eliminated by convert Fe^{2+} to Fe^{3+}; (5) we obtained the number of moles of each cation per formula unit, considering the mole fraction of Fe^{2+} relative to the sum of all divalent cations, and the mole fraction of Fe^{3+} relative to all trivalent cations.

Titanomagnetite compositional variations as a function of experimental conditions are displayed in Fig. 2. In general, titanomagnetites formed at 500 MPa show higher concentrations of Al + Mg and a slightly lower Ti content relative to crystals obtained at 0.1 MPa. As both isothermal (Fig. 2a) and quenching (Fig. 2b) temperatures are increased, the amount of Al + Mg increases, whereas the Ti content decreases. In parallel, the total iron content and the Fe^{3+}/Fe^{2+} ratio in titanomagnetite also increase (Table 2 and Fig. 2a, b).

Figure 2c shows that titanomagnetites formed under increasing cooling rate conditions are characterized by chemical trends similar to those observed as a function of temperature, except more exaggerated. Quantitatively, concentrations of Al, Mg, and Ti in titanomagnetite change by 35, 26, and 50 % with increasing cooling rate; in contrast, they change only by 6, 7, and 10 % with increasing temperature.

In Fig. 3, titanomagnetite compositions from each experimental run are plotted in the $FeO–Fe_2O_3–TiO_2$ ternary diagram. Crystals formed under both isothermal and variable quenching temperatures lie at the boundary of the Mt-Usp solid solution field. The amount of Usp progressively decreases with increasing temperature due to the lower Ti content (Fig. 2a, b). Similarly, as the cooling rate is increased, titanomagnetites from cooling rate experiments are characterized by decreasing Usp amounts. However, at the faster cooling rates, concentrations of Al + Mg are significantly higher, causing the departure from the Mt–Usp tie line (Fig. 2c).

Table 2 Representative electron microprobe analyses of experimental titanomagnetites

wt%	EB1D	EB8A	EB1E	EB7B	EB1F	EB1VF	EB2VF	EB3VF	EB4VF	EB5VF
Variable cooling rate										
TiO_2	17.87	14.51	11.15	6.11	1.07	18.22	14.93	11.64	6.71	1.78
Al_2O_3	3.09	4.70	6.31	8.72	11.14	2.26	3.93	5.60	8.10	10.61
FeO_t	72.00	72.38	72.76	73.34	73.91	73.01	73.24	73.47	73.82	74.16
FeO*	42.81	38.62	34.42	28.13	21.84	43.86	39.66	35.46	29.17	22.87
Fe_2O_3*	32.44	37.52	42.61	50.24	57.87	32.40	37.32	42.24	49.62	57.00
MnO	0.78	0.70	0.63	0.51	0.40	0.86	0.75	0.65	0.49	0.33
MgO	2.97	3.90	4.83	6.22	7.61	2.36	3.36	4.36	5.86	7.36
Tot	99.37	96.19	95.67	94.90	94.13	96.71	95.72	95.35	94.80	94.24
Tot*	99.95	99.95	99.94	99.94	99.93	99.95	99.95	99.95	99.95	99.95
Formula on the basis of 3 cations										
Ti	0.489	0.392	0.298	0.160	0.028	0.503	0.407	0.313	0.177	0.046
Al	0.133	0.199	0.264	0.359	0.451	0.098	0.168	0.236	0.335	0.431
Fe^{3+}	0.889	1.016	1.140	1.320	1.494	0.896	1.018	1.137	1.310	1.477
Fe^{2+}	1.304	1.162	1.023	0.821	0.627	1.347	1.202	1.061	0.856	0.659
Mn	0.024	0.021	0.019	0.015	0.012	0.027	0.023	0.020	0.015	0.010
Mg	0.161	0.209	0.256	0.324	0.389	0.129	0.182	0.233	0.307	0.378
FeOmol %	58.27	56.34	54.11	50.03	44.72	58.62	56.76	54.61	50.70	45.63
Fe_2O_3mol %	19.86	24.63	30.13	40.20	53.31	19.48	24.03	29.27	38.81	51.17
TiO_2mol %	21.87	19.03	15.76	9.77	1.97	21.90	19.22	16.13	10.49	3.19
Usp %	52.55	43.54	33.68	17.95	2.85	52.77	44.32	34.96	19.80	4.83

wt%	EB1D	EB12A	EB13A	EB14A	EB10A	EB11B	EB6VF	EB7VF	EB8VF	EB9VF	EB10VF	EB11VF
Variable quenching temperature												
TiO_2	17.87	17.15	16.44	15.73	15.02	14.31	18.22	17.54	16.87	16.19	15.52	14.84
Al_2O_3	3.09	3.39	3.69	3.99	4.30	4.60	2.26	2.46	2.67	2.87	3.08	3.28
FeO_t	72.00	72.07	72.13	72.20	72.26	72.33	73.01	73.12	73.23	73.33	73.44	73.55
FeO*	42.81	41.81	40.81	39.80	38.80	37.80	43.86	42.86	41.86	40.86	39.86	38.86
Fe_2O_3*	32.44	33.63	34.81	36.00	37.19	38.38	32.40	33.63	34.86	36.09	37.32	38.55
MnO	0.78	0.74	0.70	0.66	0.62	0.58	0.86	0.79	0.72	0.66	0.59	0.52
MgO	2.97	3.26	3.55	3.84	4.12	4.41	2.36	2.67	2.98	3.28	3.59	3.90
Tot	96.70	96.61	96.51	96.42	96.32	96.23	96.71	96.58	96.46	96.34	96.21	96.09
Tot*	99.95	99.98	100.00	100.02	100.05	100.07	99.95	99.95	99.95	99.95	99.95	99.95
Formula on the basis of 3 cations												
Ti	0.489	0.468	0.447	0.427	0.406	0.386	0.503	0.483	0.463	0.444	0.424	0.404
Al	0.133	0.145	0.157	0.170	0.182	0.194	0.098	0.106	0.115	0.123	0.132	0.140

Table 2 continued

wt%	EB1D	EB12A	EB13A	EB14A	EB10A	EB11B	EB6VF	EB7VF	EB8VF	EB9VF	EB10VF	EB11VF
Fe^{3+}	0.889	0.918	0.948	0.977	1.006	1.035	0.896	0.927	0.958	0.989	1.020	1.051
Fe^{2+}	1.304	1.269	1.235	1.200	1.166	1.132	1.347	1.313	1.279	1.245	1.211	1.178
Mn	0.024	0.023	0.021	0.020	0.019	0.018	0.027	0.025	0.022	0.020	0.018	0.016
Mg	0.161	0.176	0.191	0.206	0.221	0.236	0.129	0.146	0.162	0.178	0.195	0.211
FeOmol %	58.27	57.78	57.27	56.74	56.20	55.64	58.62	58.10	57.57	57.02	56.46	55.88
Fe_2O_3mol %	19.86	20.91	21.98	23.09	24.24	25.42	19.48	20.51	21.57	22.66	23.78	24.94
TiO_2mol %	21.87	21.32	20.75	20.17	19.57	18.94	21.90	21.39	20.86	20.32	19.76	19.19
Usp %	52.55	50.51	48.43	46.31	44.16	41.98	52.77	50.71	48.63	46.52	44.39	42.24

wt%	EB9A	EB17A	EB18A	EB19A	EB20A	EB21A	EB12VF	EB12VF-R	EB13VF	EB14VF	EB15VF	EB16VF	EB17VF	EB17VF-R
Variable isothermal temperature														
TiO_2	19.07	18.42	17.76	17.11	16.45	15.8	19.69	19.66	19.09	18.48	17.88	17.28	16.67	16.67
Al_2O_3	2.83	3.09	3.35	3.61	3.87	4.13	1.17	1.13	1.49	1.82	2.14	2.47	2.79	2.79
FeO_t	71.77	71.82	71.87	71.92	71.97	72.02	73.04	72.98	73	72.96	72.91	72.87	72.83	72.83
FeO*	44.71	43.76	42.81	41.86	40.91	39.96	45.45	45.37	44.57	43.7	42.83	41.96	41.08	41.08
Fe_2O_3*	30.07	31.19	32.3	33.41	34.52	35.63	30.67	30.68	31.59	32.51	33.43	34.36	35.28	35.28
MnO	0.91	0.88	0.85	0.81	0.78	0.74	0.99	0.98	0.96	0.93	0.89	0.86	0.83	0.83
MgO	2.35	2.63	2.9	3.18	3.45	3.73	2.01	2.01	2.27	2.53	2.79	3.05	3.31	3.31
Tot	96.94	96.83	96.73	96.63	96.53	96.42	96.9	96.76	96.81	96.71	96.62	96.53	96.43	96.43
Tot*	99.95	99.96	99.97	99.98	99.98	99.99	99.97	99.83	99.97	99.97	99.97	99.97	99.97	99.97
Formula on the basis of 3 cations														
Ti	0.525	0.505	0.486	0.467	0.448	0.429	0.548	0.246	0.529	0.511	0.493	0.475	0.457	0.457
Al	0.122	0.133	0.144	0.154	0.165	0.176	0.051	0.022	0.065	0.079	0.093	0.106	0.12	0.12
Fe^{3+}	0.828	0.856	0.884	0.912	0.94	0.967	0.854	0.855	0.877	0.899	0.922	0.944	0.967	0.967
Fe^{2+}	1.368	1.335	1.303	1.27	1.238	1.205	1.406	1.406	1.375	1.343	1.313	1.282	1.251	1.251
Mn	0.028	0.027	0.026	0.025	0.024	0.023	0.031	0.014	0.03	0.029	0.028	0.027	0.026	0.026
Mg	0.128	0.143	0.157	0.172	0.186	0.201	0.111	0.050	0.125	0.139	0.152	0.166	0.18	0.18
FeOmol %	59.31	58.86	58.39	57.92	57.43	56.92	59.06	59.04	58.69	58.31	57.92	57.51	57.1	57.1
Fe_2O_3mol %	17.95	18.87	19.82	20.8	21.8	22.84	17.93	17.96	18.71	19.52	20.34	21.19	22.06	22.06
TiO_2mol %	22.75	22.27	21.79	21.29	20.77	20.24	23.01	23.00	22.6	22.18	21.74	21.3	20.84	20.84
Usp %	56.62	54.74	52.83	50.89	48.91	46.91	55.26	55.16	53.83	52.36	50.84	49.29	47.7	47.7

Each composition is the average of 10 analyses reported as supplementary material is Table 1S

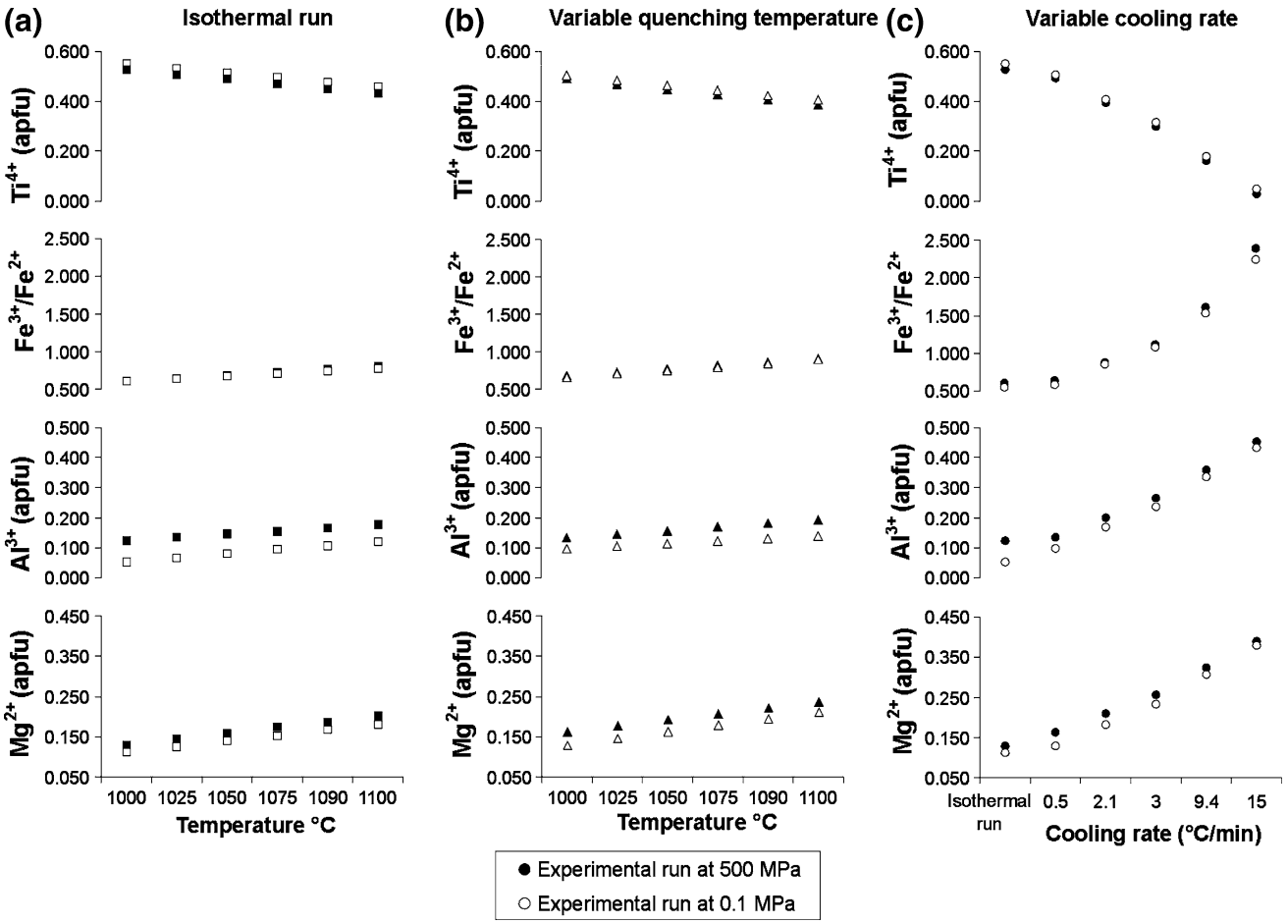

Fig. 2 Titanomagnetite compositions from isothermal runs (**a**), variable quenching temperature runs (**b**) and cooling rate runs (**c**). The titanomagnetite composition from isothermal runs at 1,000 °C are also reported for comparison in panel (**c**). Recalculation of titanomagnetite analyses is done on a 3-cation basis. Major element concentrations are reported in atoms per formula unit (apfu). *Error bars* are within symbols

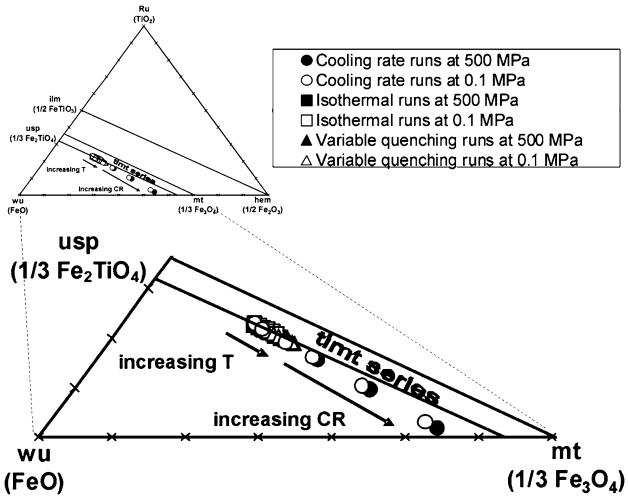

Fig. 3 Titanomagnetite compositions from experimental runs are plotted in the FeO–Fe_2O_3–TiO_2 ternary diagram. Error bars are within symbols

Discussion

Dependence of titanomagnetite composition on *P*–*T*–*X*–fO_2 and cooling rate

The crystal chemistry of titanomagnetite significantly changes in response to *P*–*T*–*X*–fO_2 variations in the melt (Spencer and Lindsley 1981; Frost et al. 1988; Andersen et al. 1991; Snyder et al. 1993; Thy and Lofgren 1994; Toplis and Carroll 1995; Thy et al. 2006); however, from a quantitative point of view, the effects induced by variable kinetic conditions are still unknown. This is surprising if we consider that the Ti content of titanomagnetites found in pillows of MORBs, lava flows, and dikes changes as a function of cooling rate (e.g. Smith and Prévot 1977; Zhou et al. 2000; Kissel et al. 2010; Mollo et al. 2011a, 2012b). Such variation alters the magnetic properties of rocks (Zhou et al. 2000 and references therein) due to mineral compositional variations lowering Ti in titanomagnetite

Table 3 Chemical analyses of natural titanomagnetites from lava flows (Tanguy et al. 1997) and dike samples (Mollo et al. 2011a)

Cooling rate	Tanguy et al. (1997)										Mollo et al. (2011a)						
#	8.0527 p1611a	5.9725 p1611PX	3.5656 p11460	0.9854 Lp1049	3.3031 p12570L	1.4853 p1170OL	Equil p1076PX	1.2069 m1076	Equil p1678PX	0.0190 m1678	Equil DK1	0.0019 DK2	0.0393 DK3	0.1067 DK4	0.2358 DK5	0.7684 DK6	1.7758 DK7
TiO_2	6.56	7.75	11.93	13.95	12.58	14.55	21.60	13.57	18.67	18.56	21.87	19.86	17.85	16.84	15.83	13.82	11.81
Al_2O_3	9.24	7.56	6.28	3.92	6.44	5.84	0.91	5.49	0.21	2.91	1.02	1.93	2.85	3.31	3.76	4.68	5.59
FeO_t	76.30	76.10	71.00	71.20	70.30	71.20	69.90	72.80	70.70	70.03	72.35	73.04	73.74	74.09	74.43	75.13	75.82
FeO*	32.72	33.73	34.58	37.78	35.17	39.71	46.91	40.25	45.14	45.17	48.82	46.87	44.92	43.95	42.98	41.03	39.08
Fe_2O_3*	48.43	47.08	40.48	37.14	39.04	35.00	25.55	36.18	28.40	27.63	26.16	29.09	32.03	33.49	34.96	37.89	40.83
MnO	0.30	0.26	0.10	0.51	0.30	0.59	1.36	0.22	0.57	0.47	0.96	0.83	0.70	0.63	0.57	0.44	0.31
MgO	3.97	3.62	5.28	3.51	5.19	3.21	1.51	2.29	0.44	1.24	1.14	1.38	1.62	1.74	1.85	2.09	2.33
Tot	96.37	95.29	94.59	93.09	94.81	95.39	95.28	94.37	90.59	93.21	97.34	97.04	96.75	96.60	96.45	96.16	95.86
Tot*	101.22	100.01	98.65	96.81	98.72	98.90	97.84	97.99	93.44	95.98	99.96	99.96	99.96	99.95	99.95	99.95	99.95
Formula on the basis of 3 cations																	
Ti	0.172	0.208	0.322	0.392	0.339	0.397	0.615	0.377	0.565	0.535	0.612	0.553	0.494	0.465	0.437	0.379	0.323
Al	0.381	0.318	0.265	0.173	0.272	0.250	0.041	0.239	0.010	0.132	0.045	0.084	0.124	0.143	0.163	0.201	0.239
Fe^{3+}	1.274	1.265	1.092	1.044	1.051	0.956	0.728	1.006	0.860	0.798	0.732	0.810	0.888	0.926	0.964	1.040	1.116
Fe^{2+}	0.957	1.008	1.036	1.180	1.053	1.205	1.487	1.244	1.519	1.449	1.518	1.451	1.384	1.351	1.318	1.252	1.187
Mn	0.009	0.008	0.003	0.016	0.009	0.018	0.044	0.007	0.019	0.015	0.030	0.026	0.022	0.020	0.018	0.014	0.009
Mg	0.207	0.193	0.282	0.195	0.277	0.174	0.085	0.126	0.026	0.071	0.063	0.076	0.089	0.095	0.101	0.114	0.126
FeOmol %	54.16	54.51	54.44	56.36	54.91	57.94	60.28	58.56	60.42	60.80	60.83	60.23	59.60	59.26	58.92	58.19	57.41
Fe_2O_3mol %	36.07	34.23	28.67	24.92	27.42	22.97	14.77	23.68	17.10	16.73	14.66	16.82	19.11	20.32	21.56	24.18	26.98
TiO_2mol %	9.77	11.26	16.89	18.71	17.66	19.09	24.96	17.76	22.47	22.47	24.51	22.95	21.29	20.42	19.52	17.63	15.60
Usp%	22.29	25.56	36.48	42.59	38.92	47.48	62.15	45.60	56.33	59.62	62.55	58.46	54.02	51.68	49.24	44.12	38.65

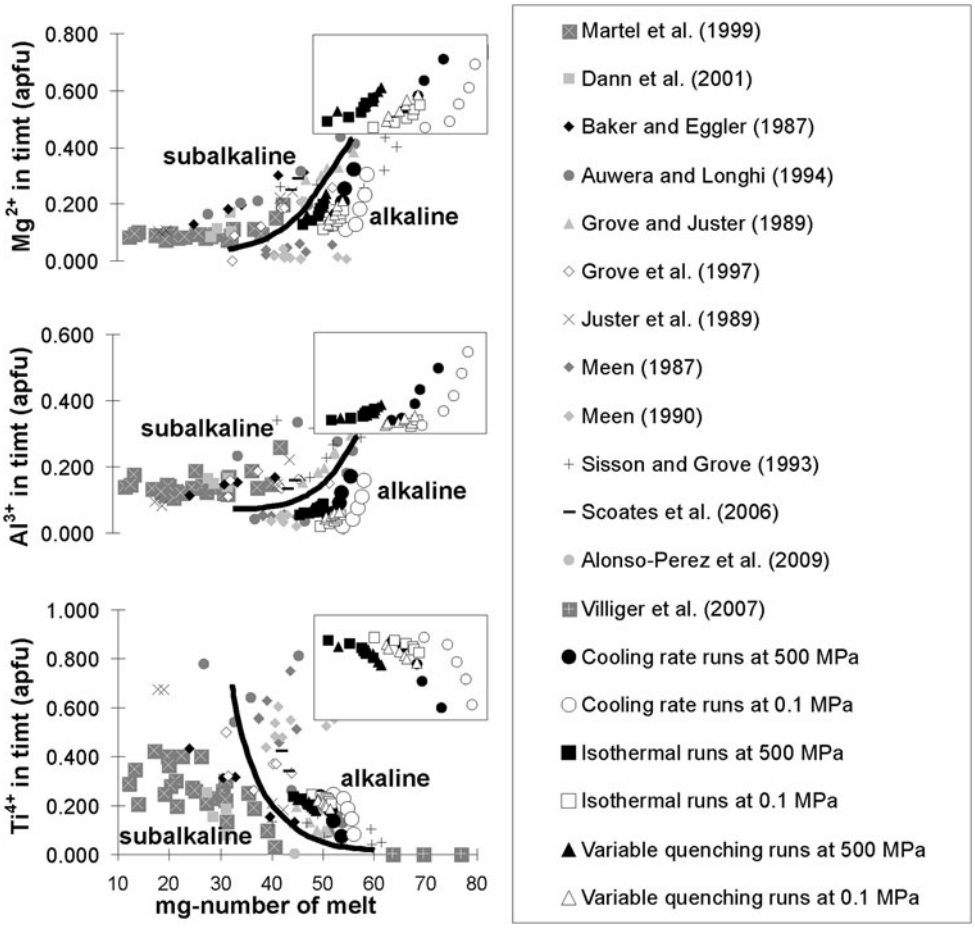

Fig. 4 Variations of Mg^{2+}, $Al^{3+,}$ and Ti^{4+} in titanomagnetite as a function of melt *mg*-number. Data from literature are compared with those from this study. Cation variations from this study are also evidenced by an accessory insert panel. *Error bars* are within symbols

and frequently counterbalanced by higher Al + Mg concentrations (Richards et al. 1994; O'Donovan and O'Reilly 1977; Chadima et al. 2009).

Therefore, our experimental results allow us to quantify for the first time the effect of cooling rate on titanomagnetite composition over temperature and pressure intervals of 1,000–1,100 °C and 0.1–500 MPa, respectively. Although the melt redox state plays a major role in determining the stability of titanomagnetite as well as the degree of solid solution between Mt and Usp (Ghiorso and Sack 1991), the constant buffering condition (NNO + 1.5) of our experiments implies that cationic substitutions in titanomagnetite observed here are necessarily related to changes in pressure, temperature, and cooling rate.

As pressure is increased from 0.1 to 500 MPa, titanomagnetite crystals are slightly enriched in Al + Mg (Fig. 2). This agrees with the observation that Mg–Al-rich spinels are characteristic of high-pressure conditions, where aluminum and magnesium are preferentially incorporated from the liquid into the crystals (Barnes and Roeder 2001 and references therein). By contrast, the amount of Ti slightly decreases with increasing pressure; notably, the Usp content does not significantly change (Table 2 and Fig. 3), confirming that temperature and oxygen fugacity mainly dictate the amount of Usp in titanomagnetite (Ghiorso and Sack 1991) in the pressure range of 0.1–500 MPa (Spencer and Lindsley 1981).

In our study, major compositional changes of titanomagnetite are observed as a function of temperature and cooling rate (Figs. 2, 3). However, chemical trends indicate that the Ti–Al–Mg cationic substitutions in titanomagnetite are mostly related to the effect of cooling rate rather than to that of temperature (Figs. 2, 3). It is worth noting that titanomagnetite compositions from our isothermal runs are comparable with to those from variable quenching experiments conducted at the slowest cooling rate of 0.5 °C/min (Fig. 2). This feature emphasizes the fact that cooling rates ≤0.5 °C/min would be slow enough to promote the nucleation and growth of titanomagnetites that closely approach equilibrium (but never fully do so). In fact, titanomagnetite compositions invariably migrate toward that of equilibrium for each quenching temperature considered (Fig. 2).

To properly assess the departure from equilibrium of titanomagnetites formed under kinetically controlled conditions, we need to have knowledge of the distribution of

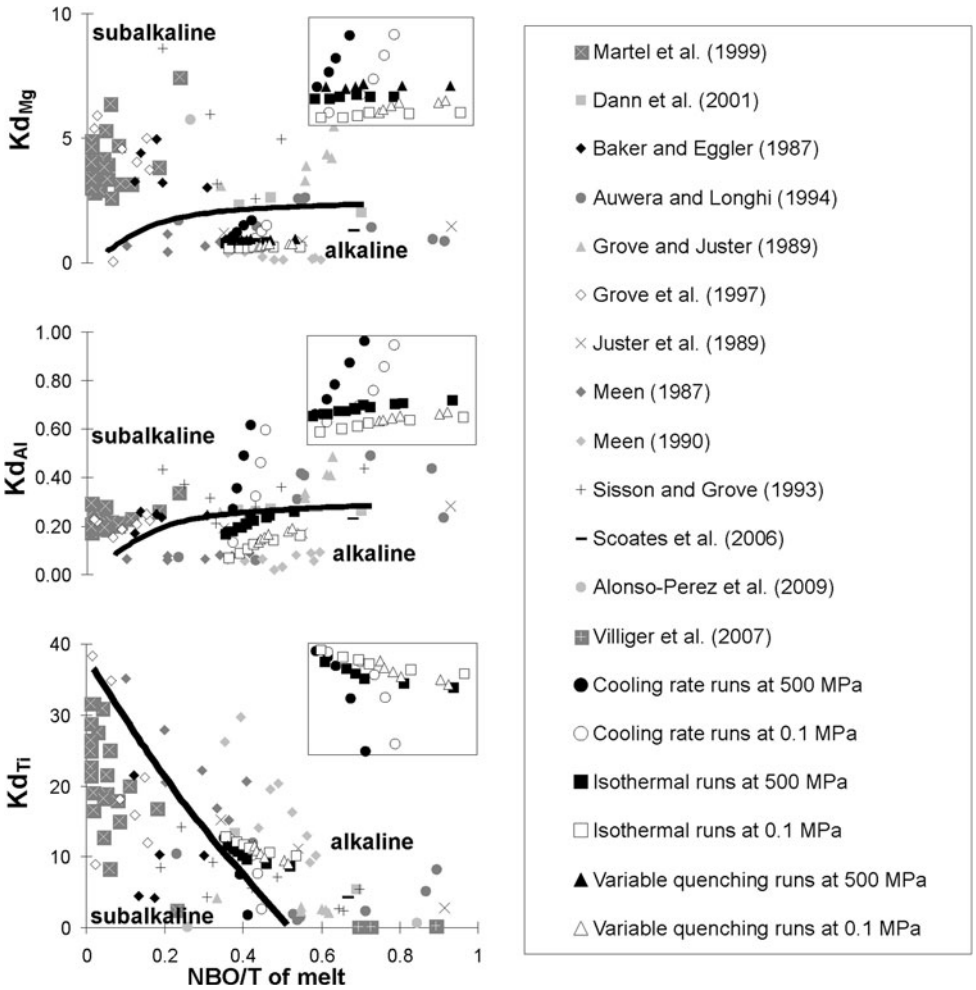

Fig. 5 Variations of Mg^{2+}, $Al^{3+,}$ and Ti^{4+} in titanomagnetite as a function of melt NBO/T (i.e. the number of non-bridging oxygens per tetrahedral cations). Data from literature are compared with those from this study. Cation variations from this study are also evidenced by an accessory insert panel. *Error bars* are within symbols

chemical components between titanomagnetite and melt under equilibrium conditions. To do this, we have selected titanomagnetite–melt pairs from several equilibrium experiments reported in the literature and conducted on both alkaline and sub-alkaline compositions (Baker and Eggler 1987; Meen 1987, 1990; Grove and Juster 1989; Juster et al. 1989; Sisson and Grove; 1993; Auwera and Longhi 1994; Grove et al. 1997; Martel et al. 1999; Dann et al. 2001; Scoates et al. 2006; Villiger et al. 2007; Alonso-Perez et al. 2009). The experiments were performed at intervals of pressure, temperature, and oxygen fugacity of 0.1–800 MPa, 876–1,210 °C, and MW-NNO + 2, respectively. The phase assemblages of the charges usually include four or five minerals plus a quenched glass; plagioclase is generally present, and ferromagnesian phases consist of olivine, orthopyroxene, clinopyroxene, and amphibole, in various combinations. Glasses span in composition from basalt to rhyolite for both alkaline and sub-alkaline series.

In Fig. 4, we plot the variation of Al, Mg, and Ti cations in titanomagnetite as a function of melt *mg*-number [*mg*-number = molar ratio of Mg/(Mg + Fe^{2+})]. Data from our experiments are also reported for comparison, and their variations are evidenced by an accessory insert panel. The compositions of glasses coexisting with titanomagnetites are reported in Table 2S available as supplementary material. Notably, we can affirm that our isothermal experiments attained equilibrium on the basis of the following observations: (1) both the amount (Table 1) and chemistry (Tables 1s and 2s) of titanomagnetites and glasses from reversal experiments do not substantially vary at isothermal conditions; (2) data reported by Mollo et al. (2010a) and based on Fe–Mg exchange between clinopyroxene and melt [$^{cpx-melt}Kd_{Fe-Mg} = (Fe^{cpx} \times Mg^{melt})/(Mg^{cpx} \times Fe^{melt})$] agree with the equilibrium value of 0.27 ± 0.03 (Putirka 1999; Putirka et al. 2003); (3) data reported by Mollo et al. (2011b) and based on the Ab–An exchange between plagioclase and melt [$^{plg-melt}Kd_{Ab-An} = {}^{plg}Ab \times {}^{melt}AlO_{1.5} \times {}^{melt}CaO)/({}^{plg}An \times {}^{melt}NaO_{0.5} \times {}^{melt}SiO_2)$] agree with the equilibrium intervals of 0.10 ± 0.05 (at $T < 1{,}050$ °C) and 0.27 ± 0.11 (at $T \geq 1{,}050$ °C) calculated by Putirka (2008); (4) silicate mineral compositions are close to those computed by the MELTS program (Ghiorso and Sack 1995) at thermodynamic equilibrium

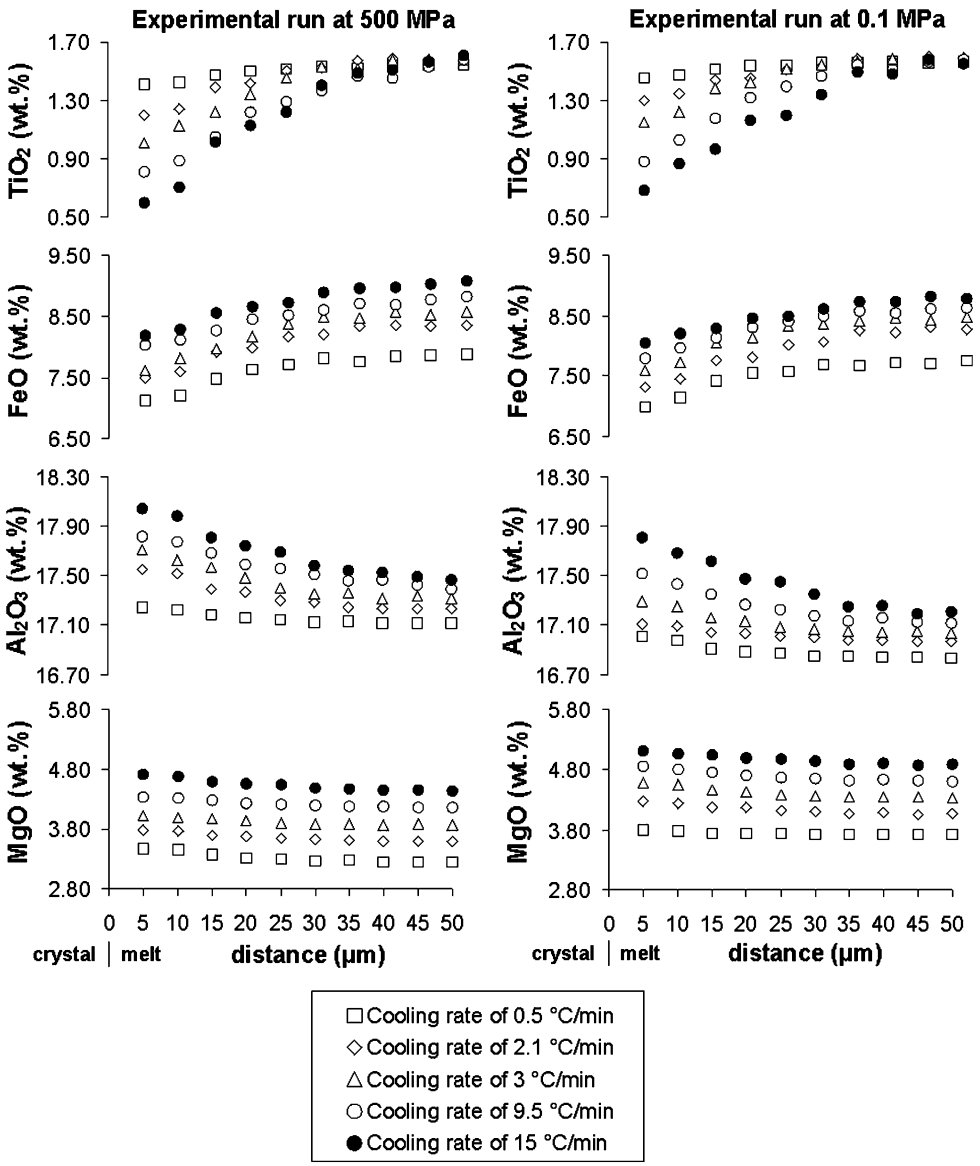

Fig. 6 Chemical profiles of TiO_2, FeO, Al_2O_3, and MgO in the melt in front of titanomagnetite crystal are shown for each cooled run. The boundary layer at crystal-melt interface becomes progressively enriched in Al_2O_3 and MgO (i.e. incompatible elements) as the cooling rate is increased; in contrast, the concentrations of TiO_2 and FeO (i.e. compatible elements) progressively decrease, also according to the melt differentiation

(cf. Mollo et al. 2010a, 2011b); (5) the duration of our isothermal experiments is substantially longer than that adopted by previous authors to obtain homogeneous phase assemblages and compositions for basaltic liquids (cf. Tormey et al. 1987 and references therein). Figure 4 shows that for a fixed *mg*-number value, titanomagnetites from subalkaline melts are characterized by higher concentrations of Al + Mg and a lower Ti content with respect to crystals from alkaline liquids. Such a feature occurs in response to a compositional control of the starting melt on the titanomagnetite crystal chemistry. In subalkaline basalts, concentrations of Al_2O_3 (15.3–17.7 wt%), and MgO (6.5–8.4 wt%) are higher, whereas the TiO_2 (0.8–2.5 wt%) content is lower relative to the amounts of Al_2O_3 (14.3–16.7 wt%), MgO (5.7–6.8 wt%), and TiO_2 (1.6–4.14 wt%) in alkaline basalts (Winter 2001 and references therein). However, Fig. 4 also highlights that, as the *mg*-number of glasses increases (i.e. as the experimental temperature is increased), the amount of Al + Mg in titanomagnetites increases; on the contrary, the Ti content decreases. Such trends agree with those observed from our equilibrium experiments (Fig. 2) and with thermodynamic computations performed through the MELTS code (Ghiorso and Sack 1995) at the *P–T–X–fO*$_2$ conditions used in this study. The Al–Mg–Ti cation redistribution has been also observed in multicomponent thermodynamic models in response to the influence of Al and Mg on the amount of Ti (Spencer and Lindsley 1981; Stormer 1983; Ghiorso and Sack 1991).

It is evident from literature data that, at the equilibrium condition, the crystal chemistry of titanomagnetite is controlled by the melt composition. Importantly, our experiments extend this finding also to titanomagnetites formed

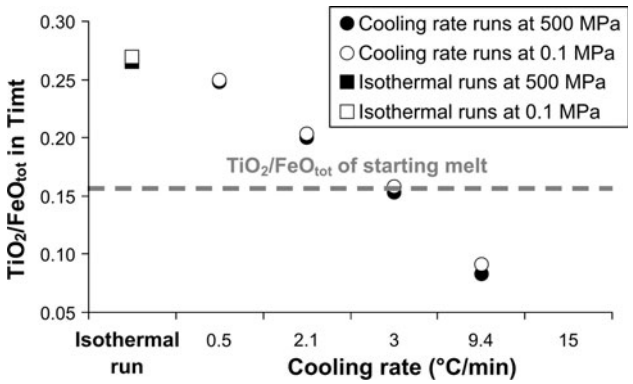

Fig. 7 The effect of equilibrium and disequilibrium growth on the TiO_2/FeO_{tot} ratio in titanomagnetite. As the cooling rate is increased, the TiO_2/FeO_{tot} ratio in titanomagnetite progressively decreases down to the TiO_2/FeO_{tot} ratio of the starting melt (0.16). *Error bars* are within symbols

under disequilibrium conditions. Since the amount of crystals progressively decreases (Table 1) with increasing cooling rate (cf. Kirkpatrick 1981), the melts are progressively less differentiated and their *mg*-number values (49–56) are higher than those (44–51) determined under isothermal temperatures (Fig. 4). Titanomagnetite compositions parallel the melt variation and, consequently, major changes of Al, Mg, and Ti are measured for crystals from rapidly cooled charges (Fig. 4). Such a feature mirrors results from recent studies demonstrating, by means of thermometric models, that early-formed microlites do not re-equilibrate with the melt over faster cooling rates, recording higher temperature compositions (Mollo et al. 2010a; Mollo et al. 2011a, b, 2012a).

In Fig. 5, we plot the titanomagnetite–melt partition coefficients determined for Al, Mg, and Ti as a function of the degree of melt polymerization. Partition coefficients are expressed as $K_i = {}^{xl}X_i/{}^{liq}X_i$ [X_i = mole fraction of i in a crystal (xl) or liquid (liq)], and they are calculated using the compositions of titanomagnetite and coexisting melt. The degree of melt polymerization is expressed as the parameter NBO/T (i.e. the number of non-bridging oxygens per tetrahedral cations) determined following the procedure reported in Mysen and Richet (2005). It has been demonstrated that the NBO/T is a powerful tool to represent the melt compositional variations under both equilibrium (Kushiro and Walter 1998; Kushiro and Mysen 2002; Mollo et al. 2010b) and disequilibrium (Mollo et al. 2011b) conditions. Moreover, since the P–T–X–fO_2 conditions of the melt do not vary simultaneously in our experiments, the individual effect of cooling rate and temperature on the melt structure can be considered isolated. Figure 5 shows that Al and Mg are generally more compatible in titanomagnetite crystals formed from subalkaline melts relative to those crystallized from alkaline liquids; the opposite occurs for Ti. Although literature data do not show well-defined trends for K_{Al} and K_{Mg}, we observe that K_{Ti} significantly decreases with increasing NBO/T. Moreover, our experimental data highlight a strict dependence of K_{Al}, K_{Mg}, and K_{Ti} with the NBO/T under both equilibrium and disequilibrium conditions (Fig. 5); however, major variations of partition coefficient are observed with increasing cooling rate. Notably, in response to the melt compositional variation, the NBO/T values (0.35–0.45) from cooling rate runs result to be lower than those (0.34–0.53) measured as a function of temperature.

The effect of cooling rate on melt composition is evidenced in Fig. 6 by means of chemical profiles measured at the crystal-melt interface (see also Table 3S available as supplementary material). The disequilibrium growth of dendritic titanomagnetites from rapidly cooled charges implies that chemical elements are rejected less efficiently into the melt next to the crystal surface (cf. Lofgren et al. 2006 and references therein) during dendritic growth compared with crystal textures resulting from closer-to-equilibrium growth. This disparity in growth versus diffusion rate (see also Kirkpatrick 1981) causes the development of a boundary layer at the titanomagnetite–melt interface enriched in elements incompatible with titanomagnetite (e.g. Al + Mg) that are then more easily incorporated into rapidly growing crystals (Figs. 2, 4, 5) compared with slowly grown crystals. As discussed in the recent studies of Baker (2008) and Watson and Müller (2009), the complex interplay between crystal growth and the element diffusivity cannot be unraveled by our experiments; in fact, a different experimental strategy is necessary to determine to what extent incompatible species are modified by chemical gradients at the crystal-melt interface as the system attempts to return to equilibrium concentrations. However, our chemical profiles highlight that, as cooling rate is increased, the amount of MgO progressively increases in the melt next to titanomagnetite crystals (Fig. 6), whereas the opposite occurs for FeO. These trends explain increased melt *mg*-numbers measured as cooling rate increases (Fig. 4). Moreover, since titanomagnetite is not an aluminosilicate mineral, both network-former (e.g. Si and Al) and network-modifier (e.g. Mg and Ca) cations increase at the crystal-melt interface (Fig. 6 and Table 3S), causing lower variations of the melt NBO/T for cooling rate runs with respect to temperature runs (Fig. 5). Figure 6 also highlights the importance of the melt composition in determining partition coefficients under disequilibrium growth conditions. Diffusion-controlled crystal growth at high cooling rates means that the crystal growth rate exceeds the ability of chemical elements to diffuse through the melt (Hammer 2008 and references therein). In this view, we obtain different titanomagnetite/melt pairs as the melt composition progressively changes toward the crystal

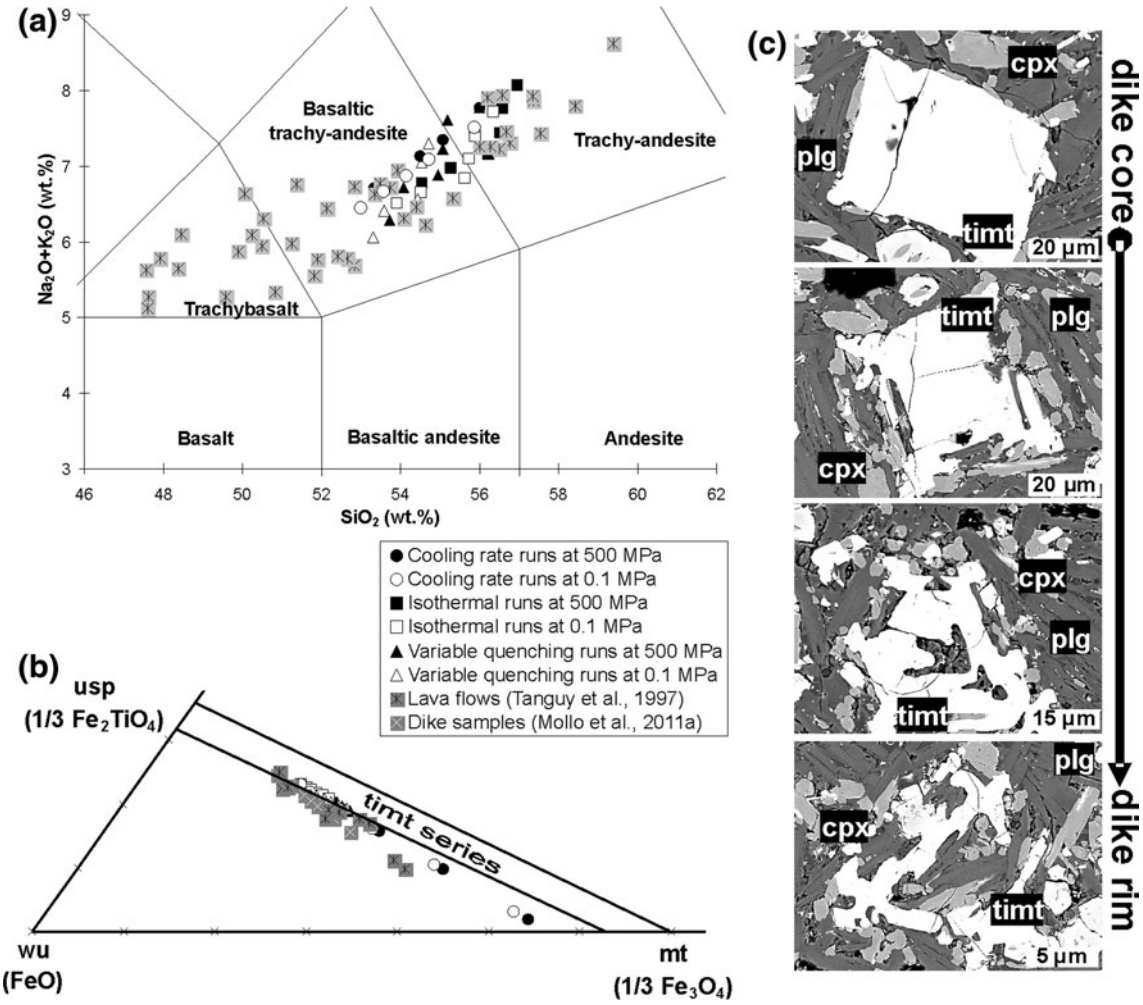

Fig. 8 In the $Na_2O + K_2O$ versus SiO_2 diagram, the melt compositions from this study are compared with the compositions of Etnean magmas (**a**). In the Usp-Wu-Mt portion of the FeO-Fe_2O_3-TiO_2 ternary diagram, the titanomagnetite compositions from this study are compared with those from Mt. Etna volcano (**b**). Textural evolution of titanomagnetite crystals found in rocks sampled from innermost to the outermost portion of a dike outcropping at Mt. Etna volcano (**c**)

surface (Fig. 6). In particular, two extremely different melt compositions can be distinguished (Fig. 6): (1) the composition of the melt next to the crystal surface, that is, the composition of the melt coexisting with the crystal rim and enriched in elements incompatible with the crystal lattice in response to a diffusion-controlled crystal growth, and (2) the composition of the residual melt far from the crystal surface, that is, the composition of the melt where chemical gradients due to a diffusion-controlled crystal growth ceases and the system returns to homogeneous concentrations. In this study, we have strictly considered the composition of the melt coexisting with the crystal surface (Fig. 6) because this liquid is enriched (or depleted) in chemical elements feeding the rapidly growing crystals. This means that, under disequilibrium conditions, the melt coexisting with the crystal surface exerts a primary control on the titanomagnetite composition.

Importantly, the compositional variation of titanomagnetites from this study allows us to experimentally demonstrate the disequilibrium growth process suggested by Zhou et al. (2000) for titanomagnetite crystals analyzed in pillow lavas with MORB affinity. These authors affirmed that the equilibrium fractionation between Ti and Fe at the crystal-melt interface causes a TiO_2/FeO_{tot} ratio (0.26) in titanomagnetite much higher than that (0.11) measured for the starting MORB composition. As the degree of cooling increases from innermost to the outermost portion of the pillow, the TiO_2/FeO_{tot} ratio in titanomagnetite progressively decreases down to the TiO_2/FeO_{tot} ratio in the starting melt. Notably, a similar behavior has been also observed for the ratio of Si/Al, Ca/Na, and Mg/Fe_{tot} in plagioclase (Iezzi et al. 2008, 2011; Mollo et al. 2011b) and clinopyroxene (Mollo et al. 2010a). According to Zhou et al. (2000), we have

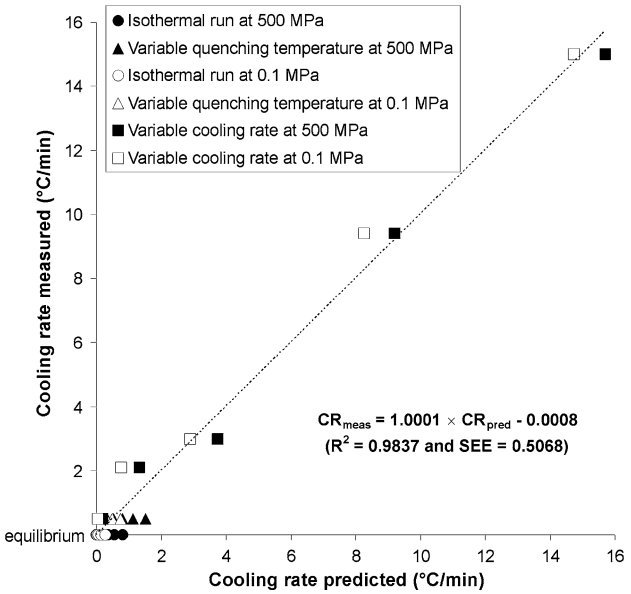

Fig. 9 Comparison between cooling rate measured (CR_{meas}) and cooling rate predicted (CR_{pred}) using the titanomagnetite-based geospeedometer from this study

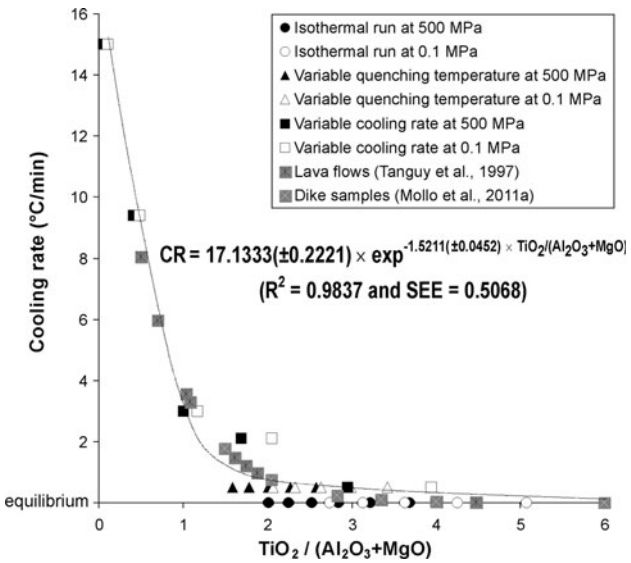

Fig. 10 Variation of $TiO/(Al_2O_3 + MgO)$ ratio in titanomagnetite as a function of cooling rate. Data from this study and from literature are plotted on the curve fitting the exponential trend

compared in Fig. 7 the TiO_2/FeO_{tot} ratio of titanomagnetites from our experiments with that of the starting trachybasaltic liquid. At the equilibrium condition, the TiO_2/FeO_{tot} ratio (0.27) in titanomagnetite is higher than that (0.16) of the melt and progressively decreases as the degree of cooling is increased (Fig. 7). Zhou et al. (2000) addressed this decreasing trend to the lower diffusivity of Ti relative to Fe in the melt during the disequilibrium growth of titanomagnetite crystals (Zhang et al. 1989). As the cooling rate is increased, diffusion cannot supply both Ti and Fe at the equilibrium proportion to the growing crystals, causing much lower Ti concentrations in the melt next to the crystal surface. Results from our experiments support this hypothesis because, as the cooling rate is increased from 0.5 to 15 °C/min, chemical profiles indicate that TiO_2 drastically decreases by 53 %, whereas FeO increases only by 13 % (Fig. 6).

To conclude, titanomagnetite compositional variations are strictly related to (1) the temperature, pressure, and melt composition (including oxygen fugacity) at the time of crystallization and (2) the kinetic control on element partitioning between titanomagnetite and melt. Undoubtedly, as it was already observed for clinopyroxene (Mollo et al. 2010a) and plagioclase (Mollo et al. 2011b and references therein), cooling rate is a powerful control on the ability of early-formed titanomagnetite crystals to equilibrate or not with the melt. Since element distributions between crystals and melt progressively depart from their equilibrium values over the effect of cooling rate, we can use this cationic substitution to calibrate a geospeedometer applicable to titanomagnetite-bearing alkaline rocks.

Implications for a geospeedometry model applicable to alkaline rocks from Mt. Etna volcano

Thermometers and oxygen barometers based on Fe–Ti oxides, that is, exchange reactions between Ti-bearing

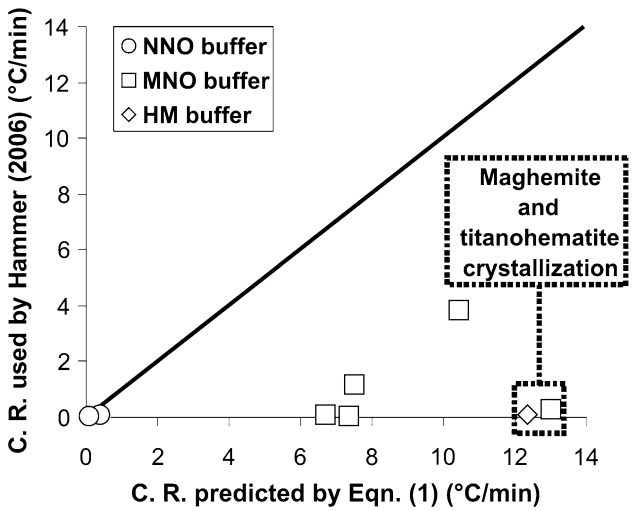

Fig. 11 Equation (1) was tested using titanomagnetite compositions reported by Hammer (2006) in Appendix T3 and obtained by cooling a tholeiitic Fe-rich basalt over a variety of redox conditions. Cooling rates (i.e. C. R.) used in laboratory are plotted versus cooling rates estimated by Eq. (1). To do this, we used the titanomagnetite compositions from run products MA-25 and MA-49 (obtained at the NNO buffer), MA-21 (obtained at the HM buffer), and MA-26, MA-34, MA-41, MA-46, and MA-50 (obtained at the MNO buffer)

magnetite and ilmenite, are commonly used for deciphering the crystallization conditions of igneous rocks (Andersen and Lindsley 1988; Andersen et al. 1991; Ghiorso and Sack 1991; Sauerzapf et al. 2008).

However, under kinetically controlled conditions, titanomagnetite occurs as a single phase and, even under the slowest cooling rates, the ulvospinel component does not exsolve out in the host titanomagnetite to form ilmenite lamellae (Buddington and Lindsley 1964). Such a feature may play an important role in the modeling of geospeedometers based on cation exchange reactions in titanomagnetite crystals. Moreover, although in tholeiitic magmas, titanomagnetite saturation drives the residual melt to the stability field of ilmenite (e.g. Snyder et al. 1993), in low-silica alkaline melts, like those from Mt. Etna volcano, ilmenite crystallization is suppressed (e.g. Carmichael et al. 1974).

Mt. Etna is the largest sub-aerial volcano in Europe, and one of the most active and intensely monitored on Earth. It represents a 1,200-km^2-wide and 3.3-km-high stratovolcano whose greater part was constructed by products associated with distinct centers of activity. Over the last 300 kyrs, Mt. Etna emitted abundant trachybasalt to basaltic trachyandesite to trachyandesite lavas, mainly characterized by the ubiquitous occurrence of clinopyroxene, plagioclase, and titanomagnetite (Tanguy et al. 1997). Petrological and geophysical studies (Métrich and Rutherford 1998; Mollo et al. 2011b, c; Heap et al. 2011) have attested that intratelluric crystals form at low-pressure conditions (500 MPa or lower) under high melt-water concentrations (1–3.5 wt%) and high oxygen fugacities (NNO–NNO + 2). Notably, simple calculations based on the fO_2 model of France et al. (2010) for alkaline rocks using the phase compositions of lava flows (Tanguy et al. 1997) and dikes (Mollo et al. 2011a) testify to high redox conditions that, as demonstrated by previous studies (Gerlach 1993; Lange and Carmichael 1996), do not significantly change even after substantial degassing, cooling, and crystallization.

Since the P–T–X–fO_2 conditions of the Mt. Etna plumbing system are very close to those used in our experiments, it is not surprising that the liquid line of descent of Etnean alkaline magmas (Tanguy et al. 1997) is faithfully reproduced by the composition of our experimental glasses (Fig. 8a). Similarly, the analyses of natural titanomagnetites in lava and dike samples from Mt. Etna volcano evidence compositional variations (Fig. 8b and Table 3) and textural evolutions (Fig. 8c) resembling those observed in this study. Notably, our experimental glasses obtained at both equilibrium and disequilibrium conditions do not reproduce the full variation of Etnean magmas (Fig. 8a). Conversely, our experimental titanomagnetites formed at the fastest cooling rate of 15 °C/min surpass the whole compositional range of natural crystals (Fig. 8b). This result underlines that rapidly growing titanomagnetite crystals from cooling lava flows may exhibit compositional variations greater than those expected at magma chamber conditions (Fig. 8b) due to incorporation of Al and Mg at the expenses of Ti (Fig. 6). We therefore take advantage of the different redistribution rates of Ti, Al, and Mg in titanomagnetite crystals from equilibrium and disequilibrium growth conditions (Figs. 2, 3, 4, 5) to calibrate a geospeedometer model for titanomagnetite-bearing alkaline rocks at Mt. Etna volcano.

Geospeedometers are based on reactions or processes whose kinetics freeze out further progresses at certain temperatures during cooling, for example, exchange reactions in crystals, and they represent an important source of information on the time–temperature paths experienced by volcanic rocks. The compositional variation of titanomagnetite crystals from this study shows that the $TiO_2/(Al_2O_3 + MgO)$ ratio changes as a function of cooling rate (CR) drawing an exponential trend fitted by the following regression:

$$CR(^{\circ}C/\mathrm{Min}) = 17.1333(\pm 0.2221) \times \exp^{-1.5211(\pm 0.0452)\times \frac{TiO_2}{(Al_2O_3+MgO)}(wt.\%)} \quad (1)$$

Equation (1) represents the first quantitative description of the effect of cooling rate on titanomagnetite composition, and it has a high precision of ±0.5068 °C/min (Fig. 9).

The titanomagnetite-bearing alkaline rocks from Mt. Etna volcano represent the best candidates to test Eq. (1). To do this, we used the titanomagnetite compositions reported in Table 3, corresponding to those of crystals analyzed in lava flows (Tanguy et al. 1997) and dike samples (Mollo et al. 2011a). Regarding the thermal history of lava flows, Eq. (1) predicts cooling rates ranging form 0.019 to 8.0527 °C/min (Table 3; Fig. 10). These values are comparable with those determined by means of relaxation geospeedometry applied to lava flows from other volcanic complexes, for example, Tenerife, Kenya, and Hawaii (Wilding et al. 1995; Gottsmann et al. 2004). The cooling rate may vary of several order of magnitude in volcanic systems; in particular, previous studies have highlighted a difference of volcanic cooling rate of four orders of magnitude (8–0.0003 °C/min) for rock samples from a relatively limited suite of volcanic facies (Wilding et al. 1995 and references therein).

On the contrary, in the case of the dike, we used titanomagnetite grains found in rock samples collected along a traverse from dike core-to-rim. Eq. (1) predicts that the cooling rate increases from 0.0019 to 1.7758 °C/min with proceeding from the innermost to the outermost portion of the dike (Table 3; Fig. 10). This cooling history is in agreement with previous estimates performed on the same

dike samples by means of (1) clinopyroxene compositional changes as a function of cooling rate (Mollo et al. 2011a) and (2) numerical simulations of thermal regimes in and around magmatic intrusions (cf. Ujike 1982; Del Gaudio et al. 2010; Mollo et al. 2011a, c).

We warn, however, that Eq. (1) may be applied only to cooling systems characterized by a redox state comparable to that (NNO + 1.5) of our experiments. To demonstrate that our geospeedometry model is not suitable for melts solidifying over buffering conditions very different from NNO + 1.5, we have tested Eq. (1) using titanomagnetite compositions reported by Hammer (2006). The author has conducted disequilibrium growth experiments on a tholeiitic Fe-rich basalt cooled from 3.85 to 0.04 °C/min over a variety of oxygen buffers. Results from our computations are presented in Fig. 11. Cooling rates predicted for titanomagnetites formed at NNO are close to those used by Hammer (2006). In contrast, cooling rate predicted at the higher redox states of MNO (i.e. MnO–Mn_3O_4 buffer) and HM (i.e. Fe_3O_4–Fe_2O_3 buffer) exhibits larger errors of estimate (Fig. 11). It is worth nothing that data affected by the highest uncertainty come from two run products in which titanomagnetite crystallized with maghemite and titanohematite, respectively. Since our geospeedometer is based on cation exchange reactions in titanomagnetite, the crystallization of multiple oxide phases causes partitioning of major crystal constituents (e.g. Ti) through paths different from those investigated in this study. Therefore, any attempt to use Eq. (1) with titanomagnetites obtained at conditions far from those of our calibration data would result in drastic overestimates (Fig. 11).

Conclusions

The following conclusions can be drawn from this study:

(i) with respect to temperature variations, cooling rate exerts a primary control on the abundance, texture, and composition of titanomagnetite;
(ii) rapidly cooled experiments show texturally immature crystals are progressively enriched in Al + Mg and depleted in Ti;
(iii) the Usp content of titanomagnetite significantly decreases in response to the disequilibrium growth conditions of the system;
(iv) the Al–Mg-Ti cation substitution in titanomagnetite is strictly dependent upon the melt composition (i.e. *mg*-number) and degree of polymerization (i.e. NBO/T);
(v) the different redistribution rates of Ti, Al, and Mg in crystals from equilibrium and disequilibrium growth conditions may be used to calibrate geospeedometers.

Acknowledgments The authors are grateful to J.E. Hammer whose accurate and useful review helped to significantly improve some important aspects of this manuscript. Thanks go to T.L. Grove for his suggestions as Editor in-chief of this journal. The manuscript was also improved as a result of constructive discussions and comments on early drafts by D.R. Baker. A. Cavallo is acknowledged for assistance during electron microprobe analysis. S. Mollo was supported by the ERC Starting grant 259256 GLASS project. This study was also supported by the "Fondi Ateneo of the University G. d"Annunzio" and the PRIN project "Experimental determination of the glass-forming ability (GFA), nucleation and crystallization of natural silicate melts" awarded to Gianluca Iezzi.

References

Alonso-Perez R, Müntener O, Ulmer P (2009) Igneous garnet and amphibole fractionation in the roots of island arcs: experimental constraints on andesitic liquids. Contrib Mineral Petrol 157(4): 541–558

Andersen DJ, Lindsley DH (1988) Internally consistent solution models for Fe-Mg-Mn-Ti oxides: Fe-Ti oxides. Am Mineral 73(7–8):714–726

Andersen DJ, Bishop FC, Lindsley DH (1991) Internally consistent solution models for Fe-Mg-Mn-Ti oxides: Fe-Mg-Ti oxides and olivine. Am Mineral 76(3–4):427–444

Auwera JV, Longhi J (1994) Experimental study of a jotunite (hypersthene monzodiorite): constraints on the parent magma composition and crystallization conditions (P, T, fO_2) of the Bjerkreim-Sokndal layered intrusion (Norway). Contrib Mineral Petrol 118:60–78

Baker DR (2008) The fidelity of melt inclusions as records of melt composition. Contrib Mineral Petrol 157(3):377–395

Baker DR, Eggler DH (1987) Compositions of anhydrous and hydrous melts coexisting with plagioclase, augite, and olivine or low Ca pyroxene from 1 atm to 8 kbar: application to the Aleutian volcanic center of Atka. Am Mineral 72(1–2):12–28

Banerjee SK (1991) Magnetic properties of Fe-Ti oxides. In: Lindsley DH (ed) Oxide Minerals: petrologic and magnetic significance. Reviews in Mineralogy, vol 25. Mineralogical Society of America, Chantilly, VA, pp 107–128

Barnes SJ, Roeder PL (2001) The range of spinel compositions in terrestrial mafic and ultramafic rocks. J Petrol 42(12):2279–2302

Bosi F, Halenius U, Skogby H (2009) Crystal chemistry of the magnetite-ulvöspinel series. Am Mineral 94(1):181–189

Bowles JA, Gee JS, Burgess K, Cooper RF (2011) Timing of magnetite formation in basaltic glass: insights from synthetic analogs and relevance for geomagnetic paleointensity analyses. Geochem Geophys Geosyst 12(2):1–18

Buddington AF, Lindsley DH (1964) Iron-titanium oxide minerals and synthetic equivalents. J Petrol 5(2):310–357

Carmichael ISE, Turner FJ, Verhoogen J (1974) Igneous petrology. McGraw–Hill, New York

Chadima M, Cajz V, Tycova P (2009) On the interpretation of normal and inverse magnetic fabric in dikes: examples from the Eger Graben, NW Bohemian Massif. Tectonophysics 466(1–2):47–63

Corsaro RA, Metrich N, Allard P, Andronico D, Miraglia L, Fourmentraux C (2009) The 1974 flank eruption of Mount Etna: an archetype for deep dike-fed eruptions at basaltic volcanoes and a milestone in Etna's recent history. J Geophys Res 114:B07204

Dann JC, Holzheid AH, Grove TL, McSween HY (2001) Phase equilibria of the Shergotty meteorite: constraints on pre-eruptive

water contents of martian magmas and fractional crystallization under hydrous conditions. Meteorit Planet Sci 36(6):793–806

Del Gaudio P, Mollo S, Ventura G, Iezzi G, Taddeucci J, Cavallo A (2010) Cooling rate induced differentiation in anhydrous and hydrous basalts at 500 MPa: implications for the storage and transport of magmas in dikes. Chem Geol 270(1–4):164–178

Dingwell DB (2006) Transport properties of magmas: diffusion and rheology. Elements 2:281–286

France L, Ildefonse B, Koepke J, Bech F (2010) A new method to estimate the oxidation state of basaltic series from microprobe analyses. J Volcanol Geoth Res 189(3–4):79–92

Freda C, Gaeta M, Misiti V, Mollo S, Dolfi D, Scarlato P (2008) Magma–carbonate interaction: an experimental study on ultrapotassic rocks from Alban Hills (Central Italy). Lithos 101:397–415

Frost BR, Lindsley DH, Andersen DJ (1988) Fe-Ti oxide-silicate equilibria: assemblages with fayalitic olivine. Am Mineral 73:727–740

Gerlach TM (1993) Oxygen buffering of Kilauea volcanic gases and the oxygen fugacity of Kilauea basalt. Geochim Cosmochim Acta 57:795–814

Ghiorso MS, Sack RO (1991) Fe-Ti oxide geothermometry: thermodynamic formulation and the estimation of intensive variables in silicic magmas. Contrib Mineral Petrol 108:485–510

Ghiorso MS, Sack RO (1995) Chemical mass transfer in magmatic processes. IV. A revised and internally consistent thermodynamic model for the interpolation and extrapolation of liquid-solid equilibria in magmatic systems at elevated temperatures and pressures. Contrib Mineral Petrol 119:197–212

Gottsmann J, Harris AJL, Dingwell DB (2004) Thermal history of Hawaiian pahoehoe lava crusts at the glass transition: implications for flow rheology and emplacement. Earth Planet Sci Lett 228:343–353

Grove TL, Juster TC (1989) Experimental investigations of low-Ca pyroxene stability and olivine-pyroxene-liquid equilibria at 1-atm in natural basaltic and andesitic liquids. Contrib Mineral Petrol 103:287–305

Grove TL, Donnelly-Nolan J, Housh T (1997) Magmatic processes that generated the rhyolite of Glass Mountain, Medicine Lake Volcano, N. California. Contrib Mineral Petrol 127:205–223

Hammer JE (2006) Influence of fO_2 and cooling rate on the kinetics and energetics of Fe-rich basalt crystallization. Earth Planet Sci Lett 248:618–637

Hammer JE (2008) Experimental studies of the kinetics and energetics of magma crystallization. In: Putirka KD, Tepley FJ (ed) Minerals, inclusions and volcanic processes. Reviews in Mineralogy and Geochemistry, vol 69. Mineralogical Society of America, Chantilly, VA, pp 9–59

Heap MJ, Baud P, Meredith G, Vinciguerra S, Bell AF, Main IG (2011) Brittle creep in basalt and its application to time-dependent volcano deformation. Earth Planet Sci Lett 307:71–82

Iezzi G, Mollo S, Ventura G, Cavallo A, Romano C (2008) Experimental solidification of anhydrous latitic and trachytic melts at different cooling rates: the role of nucleation kinetics. Chem Geol 253:91–101

Iezzi G, Mollo S, Torresi G, Ventura G, Cavallo A, Scarlato P (2011) Experimental solidification of an andesitic melt by cooling. Chem Geol 283:261–273

Jang YD, Naslund HR, McBirney AR (2001) The differentiation trend of the Skaergaard intrusion and the timing of magnetite crystallization: iron enrichment revisited. Earth Planet Sci Lett 189:189–196

Juster TC, Grove TL, Perfit MR (1989) Experimental constraints on the generation of FeTi basalts, andesites, and rhyodacites at the Galapagos Spreading Center, 85° W and 95° W. J Geophys Res 94:9251–9274

Kirkpatrick RJ (1981) Kinetics of crystallization of igneous rocks. In: Lasaga AC, Kirkpatrick RJ (ed) Kinetics of geochemical processes. Reviews in Mineralogy, vol 69. Mineralogical Society of America, Chantilly, VA, pp 321–396

Kirkpatrick RJ, Klein L, Uhlmann DR, Hays JF (1979) Rates and processes of crystal growth in the system anorthite-albite. J Geophys Res 84:3671–3676

Kissel C, Laj C, Sigurdsson H, Guillou H (2010) Emplacement of magma in Eastern Iceland dikes: insights from magnetic fabric and rock magnetic analyses. J Volcanol Geotherm Res 191:79–92

Kushiro I, Mysen BO (2002) A possible effect of melt structure on the $Mg–Fe^{2+}$ partitioning between olivine and melt. Geochim Cosmochim Acta 66:2267–2272

Kushiro I, Walter MJ (1998) Mg–Fe partitioning between olivine and mafic-ultramafic melts. Geophys Res Lett 25:2337–2340

Lange RA, Carmichael ISE (1996) The Aurora volcanic field, California-Nevada: oxygen fugacity constraints on the development of andesitic magma. Contrib Mineral Petrol 125:167–185

Lattard D, Engelmann R, Kontny A, Sauerzapf U (2006) Curie temperatures of synthetic titanomagnetites in the Fe-Ti-O system. Reassessment of some methodological and crystal chemical effects. J Geophys Res 111:B12S28

Lofgren GE, Huss GR, Wasserburg GJ (2006) An experimental study of trace-element partitioning between Ti-Al-clinopyroxene and melt: equilibrium and kinetic effects including sector zoning. Am Mineral 91:1596–1606

Martel C, Pichavant M, Holtz F, Scaillet B, Bourdier J-L, Traineau H (1999) Effects of fO_2 and H_2O on andesite phase relations between 2 and 4 kbar. J Geophys Res 104:29453–29470

Meen JK (1987) Formation of shoshonites from calcalkaline basalt magmas: geochemical and experimental constraints from the type locality. Contrib Miner Petrol 97(3):333–351

Meen JK (1990) Elevation of potassium content of basaltic magma by fractional crystallization: the effect of pressure. Contrib Mineral Petrol 104:309–331

Métrich N, Rutherford MJ (1998) Low pressure crystallization paths of H_2O-saturated basaltic-hawaiitic melts from Mt Etna: implications for open-system degassing of basaltic volcanoes. Geochim Cosmochim Acta 62:1195–1205

Mollo S, Del Gaudio P, Ventura G, Iezzi G, Scarlato P (2010a) Dependence of clinopyroxene composition on cooling rate in basaltic magmas: implications for thermobarometry. Lithos 118:302–312

Mollo S, Gaeta M, Freda C, Di Rocco T, Misiti V, Scarlato P (2010b) Carbonate assimilation in magmas: a reappraisal based on experimental petrology. Lithos 114:503–514

Mollo S, Lanzafame G, Masotta M, Iezzi G, Ferlito C, Scarlato P (2011a) Cooling history of a dike as revealed by mineral chemistry: a case study from Mt. Etna volcano. Chem Geol 288:39–52

Mollo S, Putirka K, Iezzi G, Del Gaudio P, Scarlato P (2011b) Plagioclase-melt (dis)equilibrium due to cooling dynamics: implications for thermometry, barometry and hygrometry. Lithos 125:221–235

Mollo S, Vinciguerra S, Iezzi G, Iarocci A, Scarlato P, Heap MJ, Dingwell DB (2011c) Volcanic edifice weakening via devolatilization reactions. Geophys J Int 186:1073–1077

Mollo S, Misiti V, Scarlato P, Soligo M (2012a) The role of cooling rate in the origin of high temperature phases at the chilled margin of magmatic intrusions. Chem Geol 322–323:28–46

Mollo S, Iezzi G, Ventura G, Cavallo A, Scarlato P (2012b) Heterogeneous nucleation mechanisms and formation of metastable phase assemblages induced by different crystalline seeds in a rapidly cooled andesitic melt. J Non-Cryst Sol 358:1624–1628

Muncill GE, Lasaga AC (1987) Crystal-growth kynetics of plagioclase in igneous systems: one atmosphere experiments and approximation of a simplified growth model. Am Mineral 72:299–311

Mysen BO, Richet P (2005) Silicate glasses and melts: properties and structure. Developments in geochemistry, vol 10. Elsevier, Amsterdam, p 544

O'Reilly W (1984) Rock and mineral magnetism. Blackie, Glasgow, p 220

O'Donovan JB, O'Reilly W (1977) Range of non-stoichiometry and characteristic properties of the products of laboratory maghemitization. Earth Planet Sci Lett 34:291–299

Pearce CI, Henderson CMB, Telling ND, Pattrick RAD, Charnock JM, Coker VS, Arenholz E, Tuna F, van der Laan G (2010) Fe site occupancy in magnetite-ulvöspinel solid solutions: a new approach using X-ray magnetic circular dichroism. Am Mineral 95:425–439

Pick T, Tauxe L (1994) Characteristics of magnetite in submarine basaltic glass. Geophys J Int 119:116–128

Putirka K (1999) Clinopyroxene + liquid equilibria. Contrib Min Pet 135:151–163

Putirka KD (2008) Thermometers and barometers for volcanic systems. In: Putirka KD, Tepley F (Eds) Minerals, inclusions, and volcanic processes: reviews in mineralogy and geochemistry, vol 69. pp 61–120

Putirka K, Ryerson FJ, Mikaelian H (2003) New igneous thermobarometers for mafic and evolved lava compositions, based on clinopyroxene + liquid equilibria. Am Min 88:542–1554

Putnis A (1992) Introduction to mineral sciences. Cambridge University Press, Cambridge, p 206

Richards JCW, O'Donovan JB, Hauptman Z, Pick T, Tauxe L (1994) Characteristics of magnetite in submarine basaltic glass. Geophys J Int 119:116–128

Richet P (2002) Enthalpy, volume and structural relaxation in glass-forming silicate melts. J Therm Anal Calorim 69:739–750

Sauerzapf U, Lattard D, Burchard M, Engelmann R (2008) The titanomagnetite-ilmenite equilibrium: new experimental data and thermooxybarometric application to the crystallization of basic to intermediate rocks. J Petrol 49:1161–1185

Scaillet B, Evans BW (1999) The 15 June 1991 eruption of Mount Pinatubo. I. Phase quilibria and pre-eruption P-T-fO_2-fH_2O conditions of the dacite magma. J Petrol 40:381–411

Scoates JS, Lo Cascio M, Weis D, Lindsley DH (2006) Experimental constraints on the origin and evolution of mildly alkalic basalts from the Kerguelen Archipelago, Southeast Indian Ocean. Contrib Mineral Petrol 151:582–599

Sisson TW, Grove TL (1993) Experimental investigations of the role of H_2O in calc-alkaline differentiation and subduction zone magmatism. Contrib Mineral Petrol 113:143–166

Smith BM, Prévot M (1977) Variation of the magnetic properties in a basaltic dyke with concentric cooling zones. Phys Earth Planet Int 14:120–136

Snyder D, Carmichael ISE, Wiebe RA (1993) Experimental study of liquid evolution in an Fe-rich, layered mafic intrusion: constraints of Fe–Ti oxide precipitation on the T-fO_2 and T-ρ paths of tholeiitic magmas. Contrib Mineral Petrol 113:73–86

Spencer KJ, Lindsley DH (1981) A solution model for coexisting iron-titanium oxides. Am Mineral 66:1189–1201

Stormer JC Jr (1983) The effects of recalculation on estimates of temperature and oxygen fugacity from analyses of multicomponent iron-titanium oxides. Am Mineral 68:586–594

Tanguy JC, Condomines M, Kieffer G (1997) Evolution of the Mount Etna magma: constraints on the present feeding system and eruptive mechanism. J. Volcanol Geotherm Res 75:221–250

Thy P, Lofgren GE (1994) Experimental constraints on the low-pressure evolution of transitional and mildly alkalic basalts: the effect of Fe-Ti oxide minerals and the origin of basaltic andesites. Contrib Mineral Petrol 116:340–351

Thy P, Lesher CE, Nielsen TFD, Brooks CK (2006) Experimental constraints on the Skaergaard liquid line of descent. Lithos 92:154–180

Toplis MJ, Carroll MR (1995) An experimental study of the influence of oxygen fugacity on Fe–Ti oxide stability, phase relations, and mineral-melt equilibria in ferro-basaltic systems. J Petrol 36:1137–1170

Tormey DR, Grove TL, Bryan WB (1987) Experimental petrology of normal MORB near the Kane Fracture Zone: 22°–25° N, mid-Atlantic ridge. Contrib Mineral Petrol 96:121–139

Tsuchiyama A (1983) Crystallization kinetics in the system CaMgSi$_2$O$_6$-CaAl$_2$Si$_2$O$_8$: the delay in nucleation of diopside and anorthite. Am Mineral 68:687–698

Ujike O (1982) Microprobe mineralogy of plagioclase, clinopyroxene and amphibole as records of cooling rate in the Shirotori-Hiketa dike swarm, northeastern Shikoku, Japan. Lithos 15:281–293

Villiger S, Ulmer P, Müntener O (2007) Equilibrium and fractional crystallization experiments at 0.7 GPa—The effect of pressure on phase relations, liquid compositions and mineral-liquid exchange reactions of tholeiitic magmas. J Petrol 48:159–184

Watson EB, Müller T (2009) Non-equilibrium isotopic and elemental fractionation during diffusion-controlled crystal growth under static and dynamic conditions. Chem Geol 267:111–124

Webb SL (2005) Silicate melts at extreme conditions: In: Miletich R (ed) EMU Notes in Mineralogy, vol 7. pp 64–95

Wilding MC, Webb SL, Dingwell DB (1995) Evaluation of a relaxation geospeedometer for volcanic glasses. Chem Geol 125:137–148

Winter JD (2001) An introduction to igneous and metamorphic petrology. Upper Saddle River, Prentice Hall, NJ, p 695

Zhang Y, Walker D, Lesher CE (1989) Diffusive crystal dissolution. Contrib Mineral Petrol 102:492–513

Zhou W, Van der Voo R, Peacor DR, Zhang Y (2000) Variable Ti-content and grain size of titanomagnetite as a function of cooling rate in very young MORB. Earth Planet Sci Lett 179:9–20